Supplementary Information: Tunable Electrocaloric Effect in Lead Scandium Tantalate through Calcium Doping

Youri Nouchokgwe*[1,2], Natalya S. Fedorova[1,2], Veronika Kovacova[1,2], Pranab Biswas[2,3], Ivana Gorican[4], Nejc Suban[4], Silvo Drnovsek[4], Matej Sadl[4], Michele Melchiorre[3], Binayak Mukherjee[1,2], Uros Prah[1,2], Guillaume F. Nataf[5], Torsten Granzow[1,2], Mael Guennou[2,3], Hana Ursic[4], Jorge Iñiguez-Gonzalez[1,2,3], and Emmanuel Defay*[1,2,3]

[1] *Smart Materials Research Unit, Luxembourg Institute of Science and Technology, Maison des Matériaux, 28 Av. des Hauts Fourneaux, L-4362 Esch-Belval, Esch-sur-Alzette.*

[2] *Inter-institutional Research Group University of Luxembourg - LIST on Ferroic Materials,41 rue du Brill, L-4422 Belvaux, Luxembourg*

[3] *Department of Physics and Materials Science, University of Luxembourg, L-4422 Belvaux, Luxembourg*

[4] *Jožef Stefan Institute, Jamova cesta 39, Ljubljana 1000, Slovenia*

[5] *GREMAN UMR7347, CNRS, University of Tours, INSA Centre Val de Loire, 37000 Tours, France*

[*] *corresponding authors: youri.nouchokgwe@list.lu ; emmanuel.defay@list.lu*

November 5, 2025

Contents

Supplementary Note 1: Grain size of calcium-doped PST

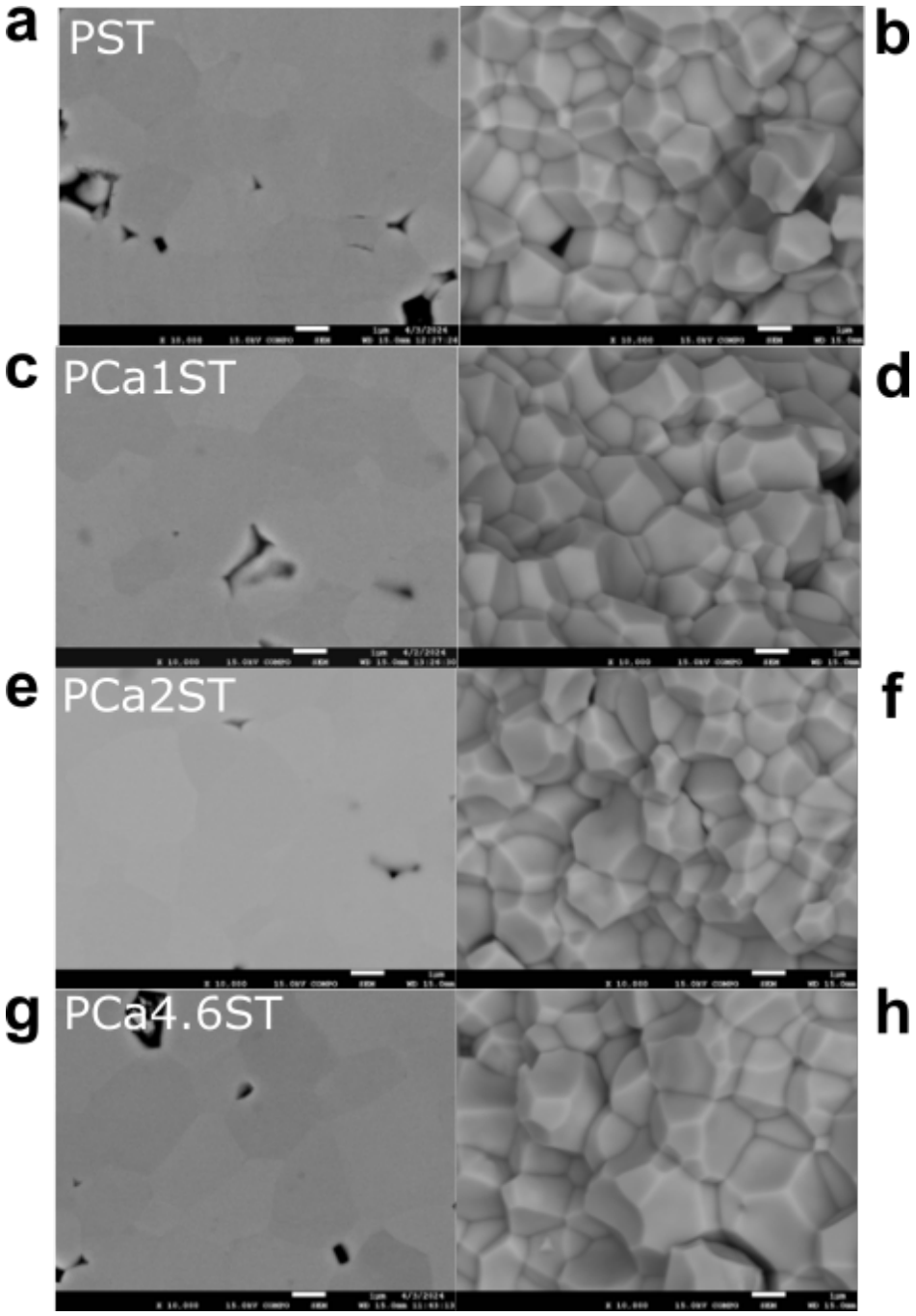

Supplementary Figure 1: **SEM Images of PCaxST.** (a), (b), (c), and (d) are respectively the SEM images of PST, PCa1ST, PCa2ST, and PCa4.6ST.

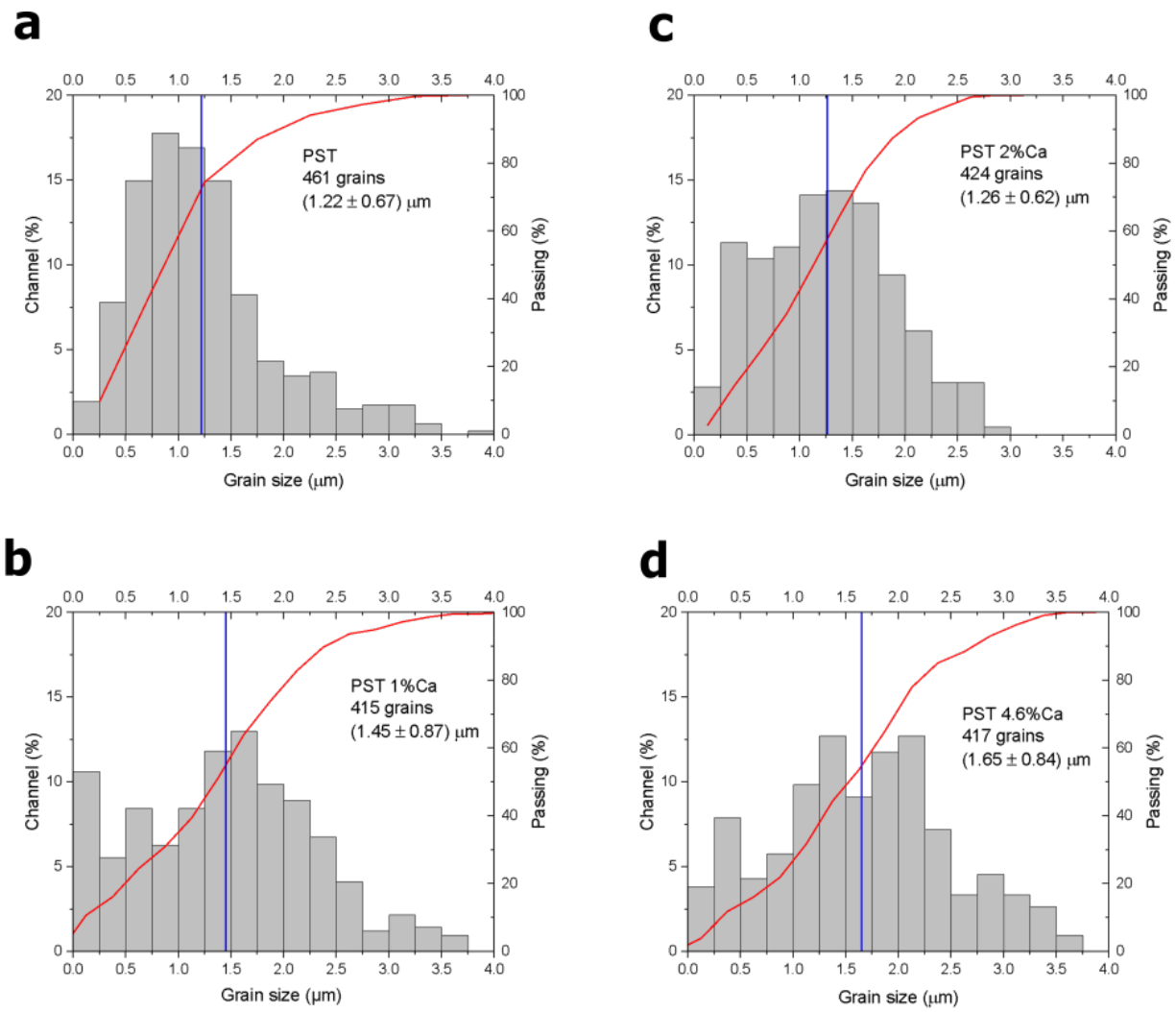

Supplementary Figure 2: **Grain size of PxCaST.** (a), (b), (c), and (d) are respectively the grain size calculation of respectively PST, PCa1ST, PCa2ST, and PCa4.6ST. It was determined by analyzing digitalized microstructure images in Image Tool software (version 3.0, United States).

Supplementary Note 2: XRD of calcium-doped PST

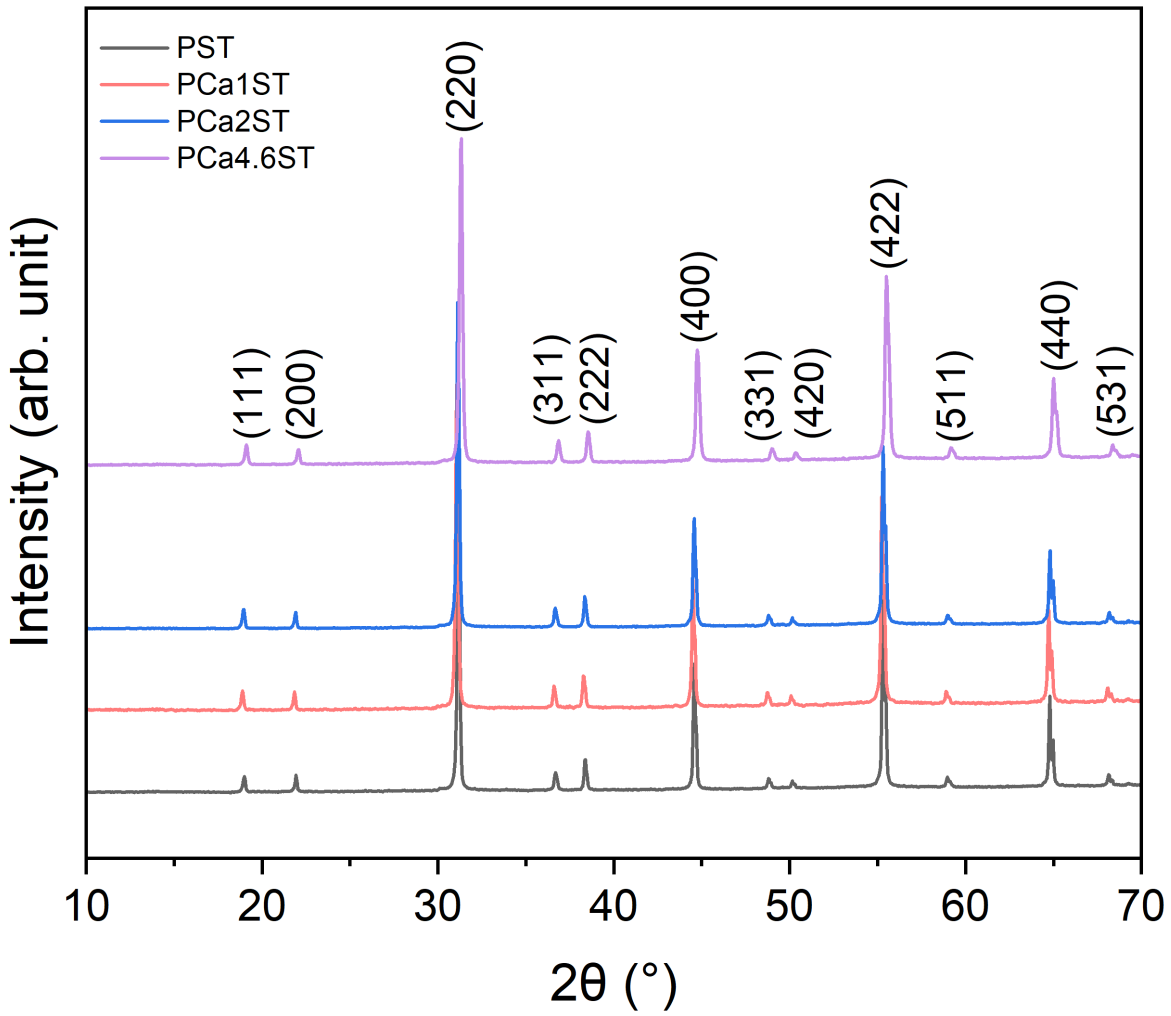

Supplementary Figure 3: **XRD of PCaxST.** The XRD measurements were carried out at 50℃ (in the cubic phase).

Supplementary Note 3: Structure of calcium-doped PST

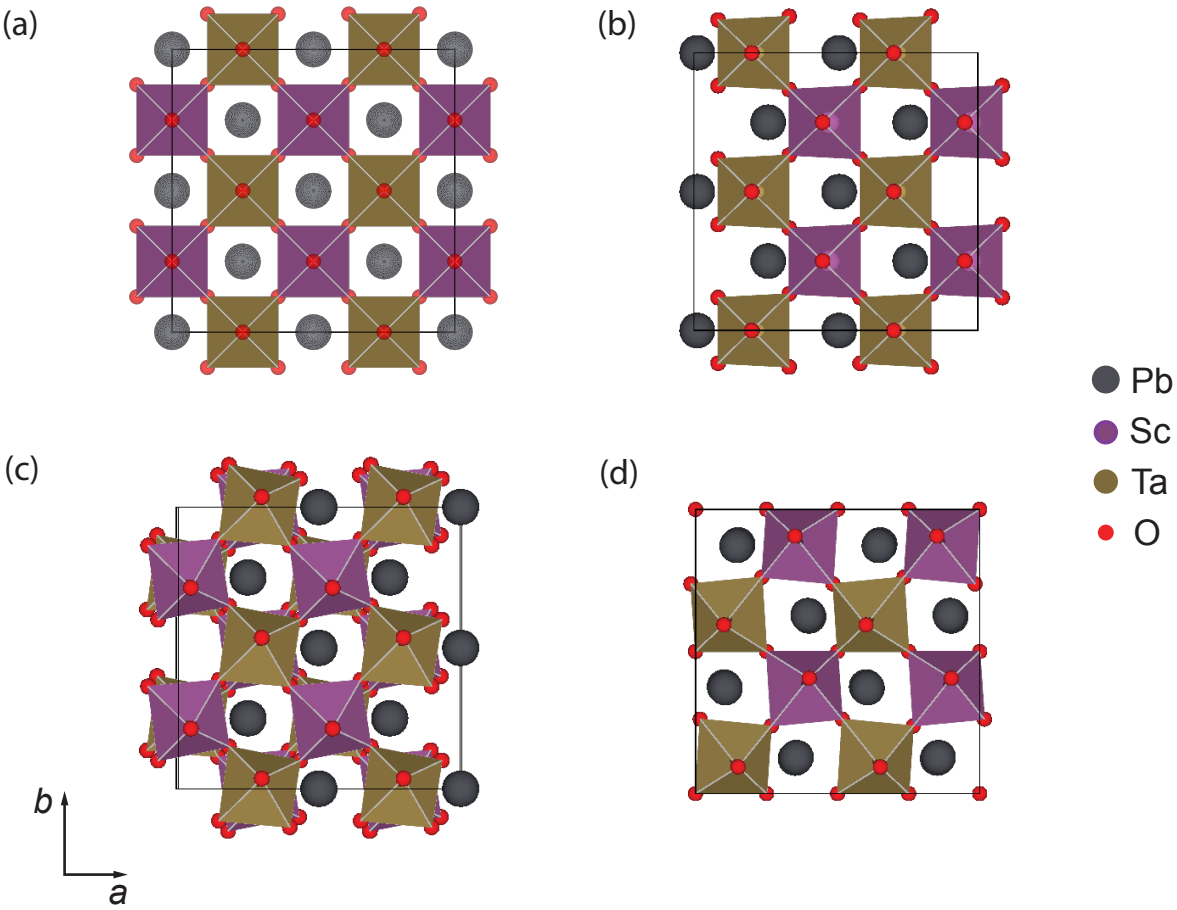

Supplementary Figure 4: **Structural polymorphs of pure PST considered in this work.** Panels (a), (b), (c) and (d) show c, rI, rII and AFE polymorphs, respectively. The lattice vectors *asc*, *bsc* and *csc* of the 80 atom cells are related to the *ap*, *bp* and *cp* lattice vectors of 5-atom perovskite cell as follows: $a_{sc} = 2a_p + 2b_p$; $b_{sc} = -2a_p + 2b_p$; $c_{sc} = 2c_p$.

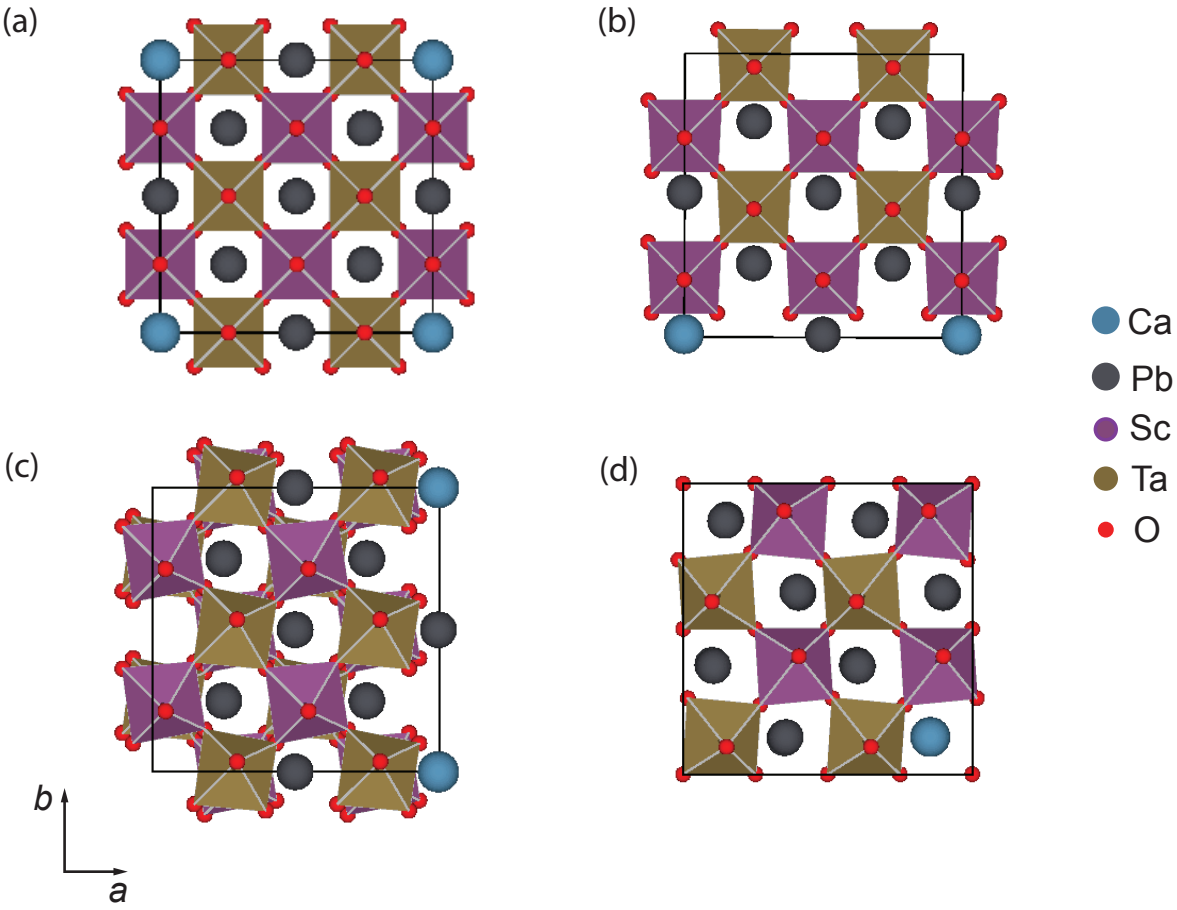

Supplementary Figure 5: **Structural polymorphs of PST doped with 6.25% of Ca considered in this work.** Panels (a), (b), (c) and (d) show c, rI, rII and AFE polymorphs, respectively.

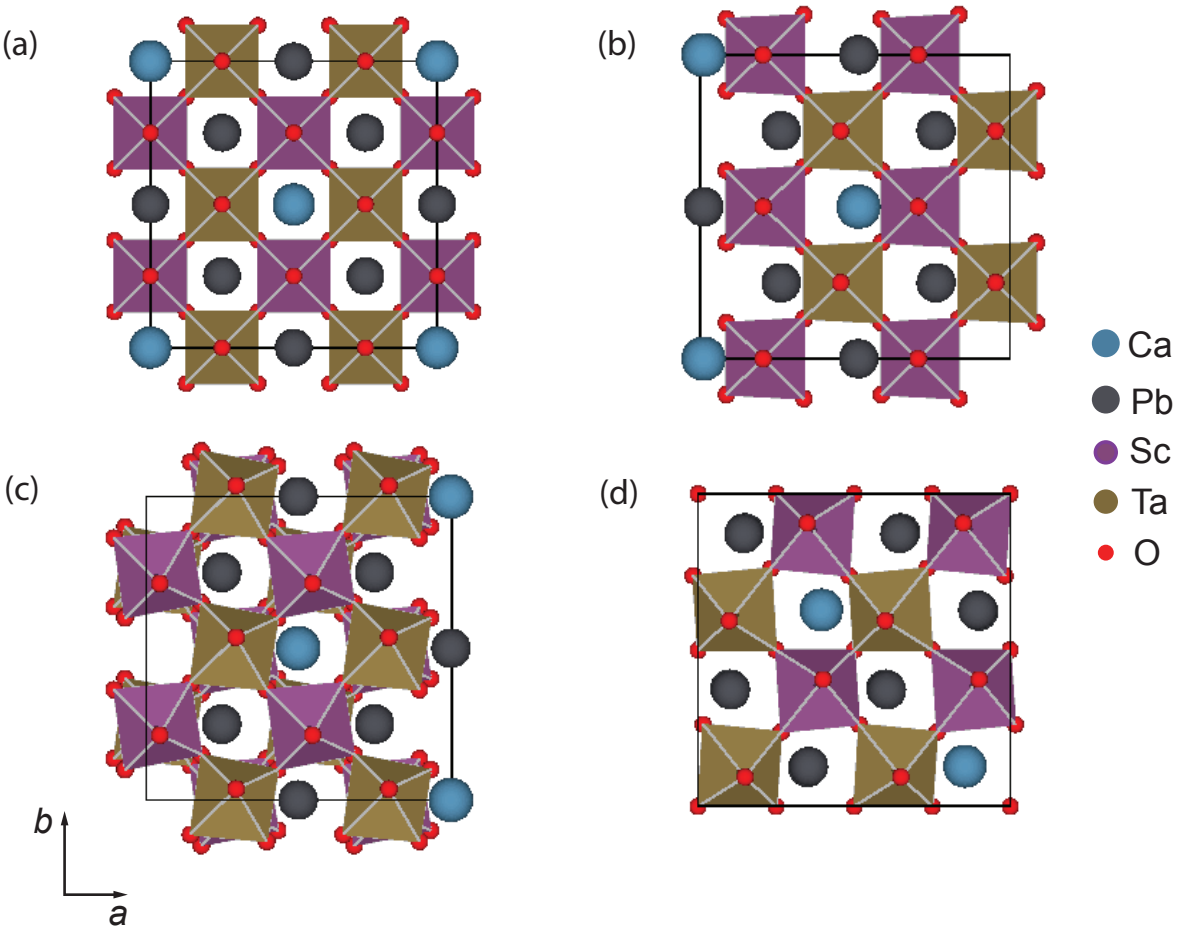

Supplementary Figure 6: **Structural polymorphs of PST doped with 12.5% of Ca considered in this work.** Panels (a), (b), (c) and (d) show c, rI, rII and AFE polymorphs, respectively.

Supplementary Note 4: Simulated XRD pattern of undoped PST

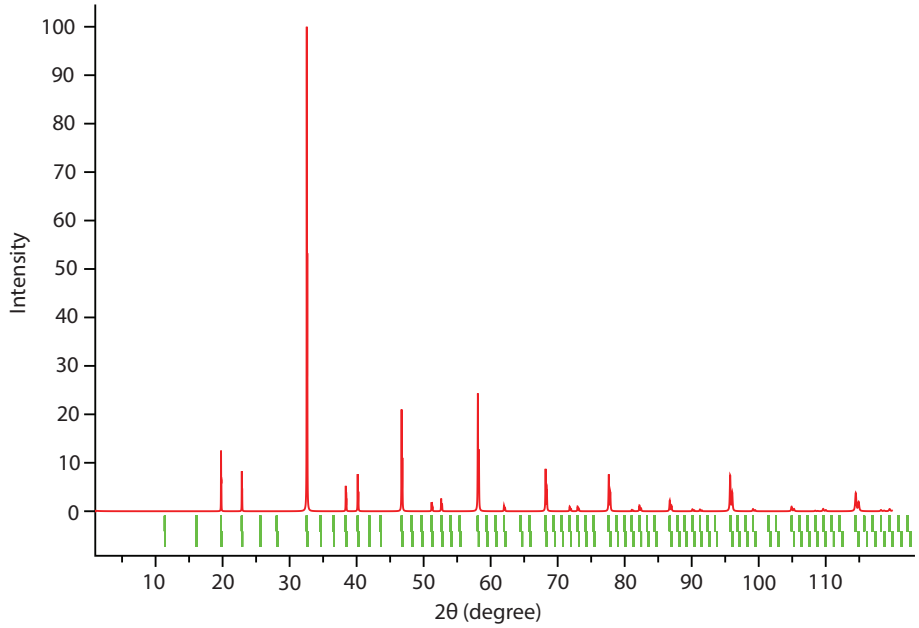

Supplementary Figure 7: **Theoretical XRD pattern obtained for cubic phase of pure PST with perfect Sc/Ta ordering.**

Supplementary Table 1: **Intensity ratio I_{111}/I_{200} calculated for cubic phase of pure and Ca-doped PST with perfect Sc/Ta order.**

Ca Concentration	I_{111}/I_{200}
0%	1.37
1.56%	1.47
3.125%	1.59
12.5%	2.60

Supplementary Note 5: Polarization versus electric field loops of calcium-doped PST

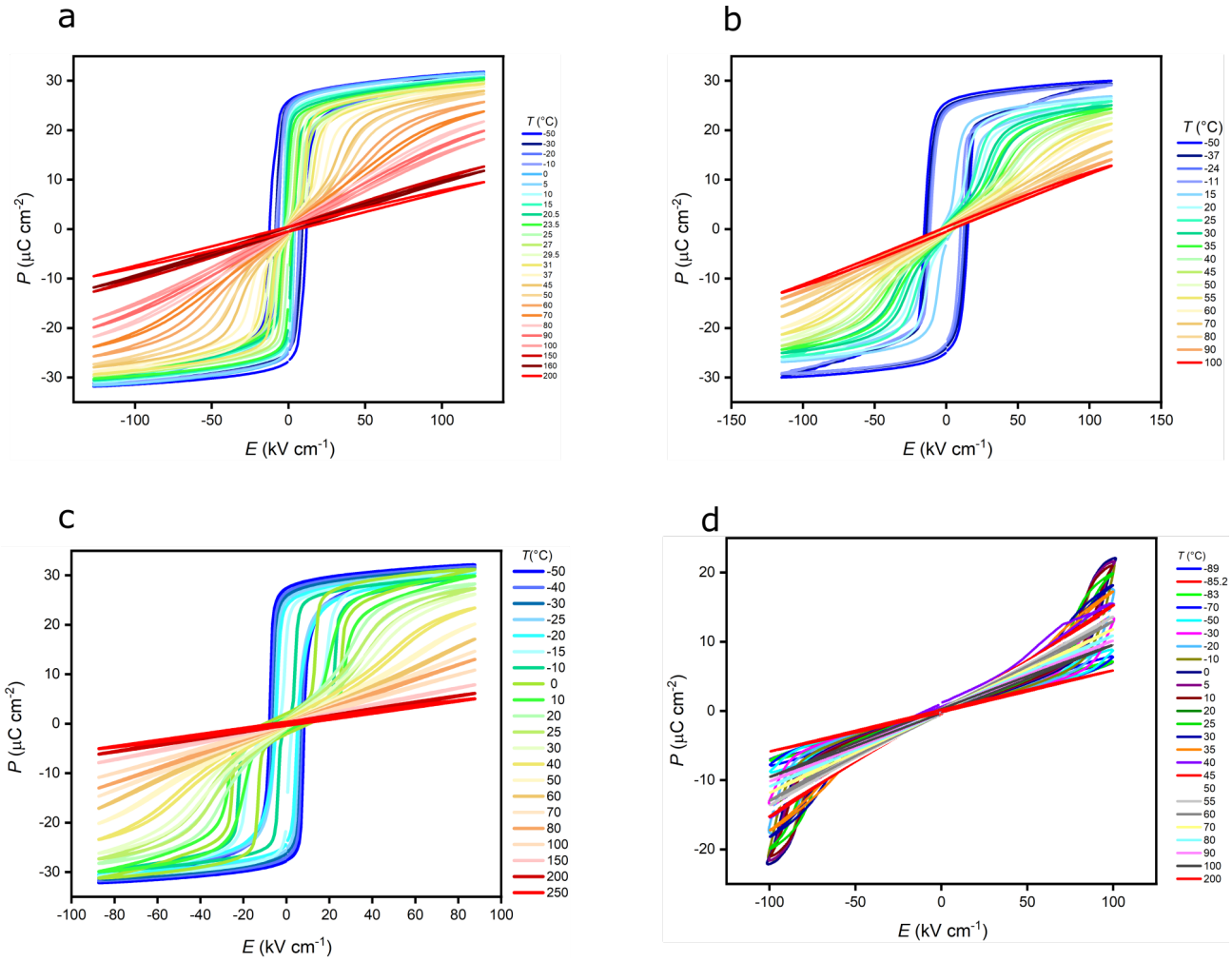

Supplementary Figure 8: **PE loops of PCaxST** a) pure PST. b) PCa1ST. c) PCa2ST. d) PCa4.6ST.

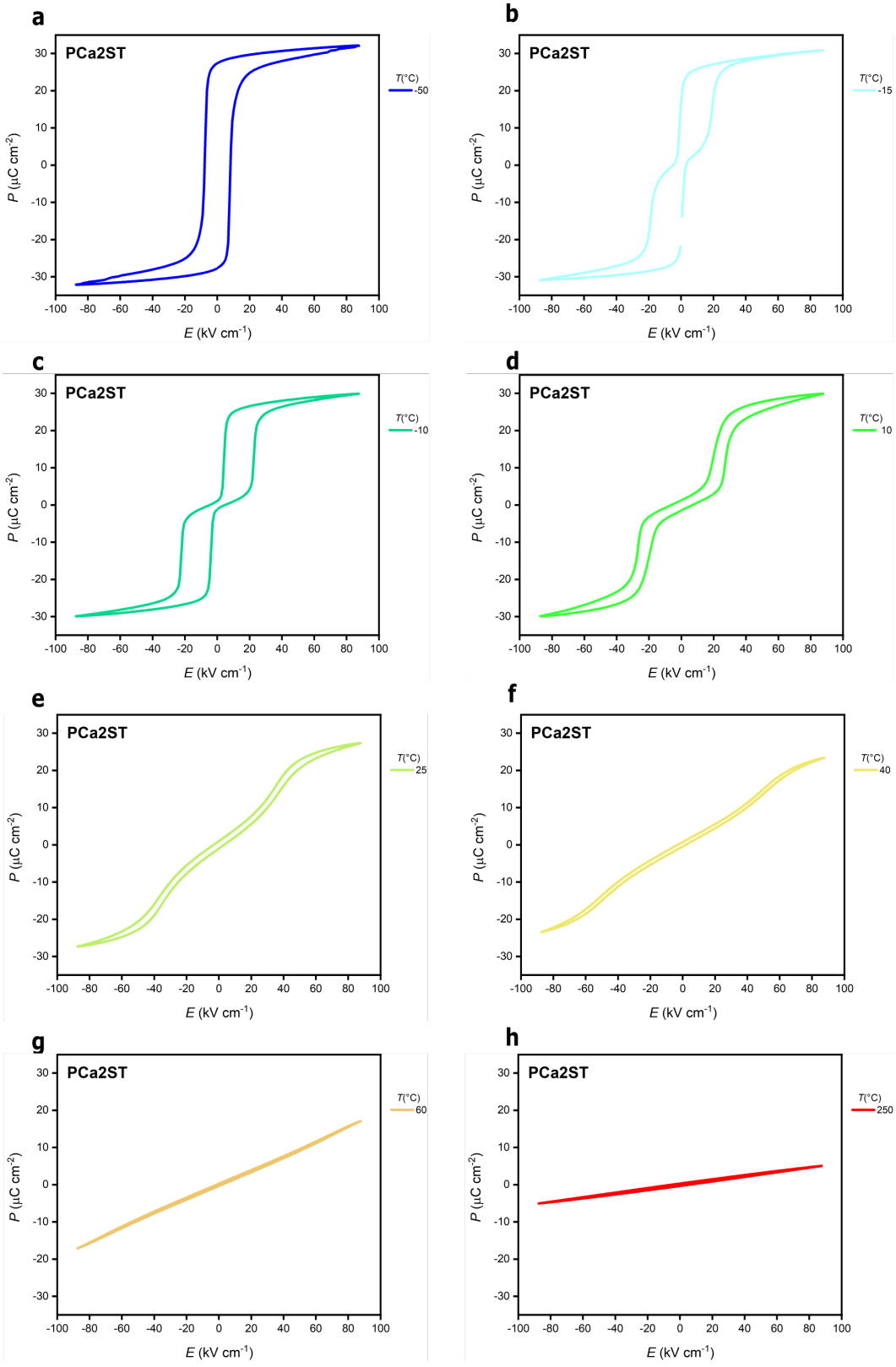

Supplementary Figure 9: **Temperature dependence of polarization loops of 2%Ca-doped PST.** a) -50℃, the material is FE b) -15℃, the material transitions to an AFE c) -10℃, the material is AFE, d) 10℃ and e) 25℃, the material transitions to a PE f) 40℃, g) 60℃, h) 250℃.

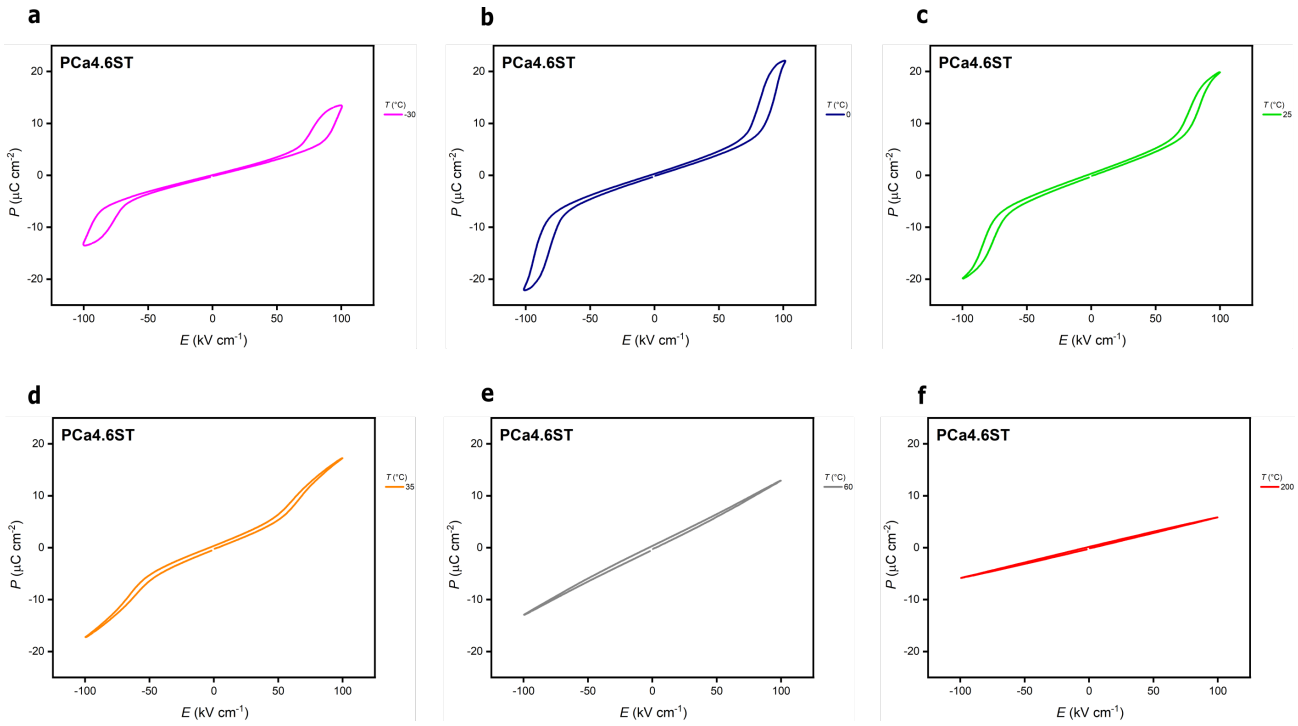

Supplementary Figure 10: **Temperature dependence of polarization loops of 4.6%Ca-doped PST.** a) -30℃, b) 0℃, c)25℃, d) 35℃ and e) 60℃ and f) 200℃.

Supplementary Note 6: Dielectric measurements

In this Supplementary Note, we present dielectric measurements collected at 1 kHz for Ca-doped PST samples during both heating and cooling at a rate of 1 K/min. The measured transition temperatures are consistent with those obtained from DSC. More specifically, in PCa2ST we observe a shoulder around $-17\,^{\circ}\mathrm{C}$, which coincides with the field-induced FE-AFE transition identified by *in-situ* field DSC (Figures 1c and 3c).

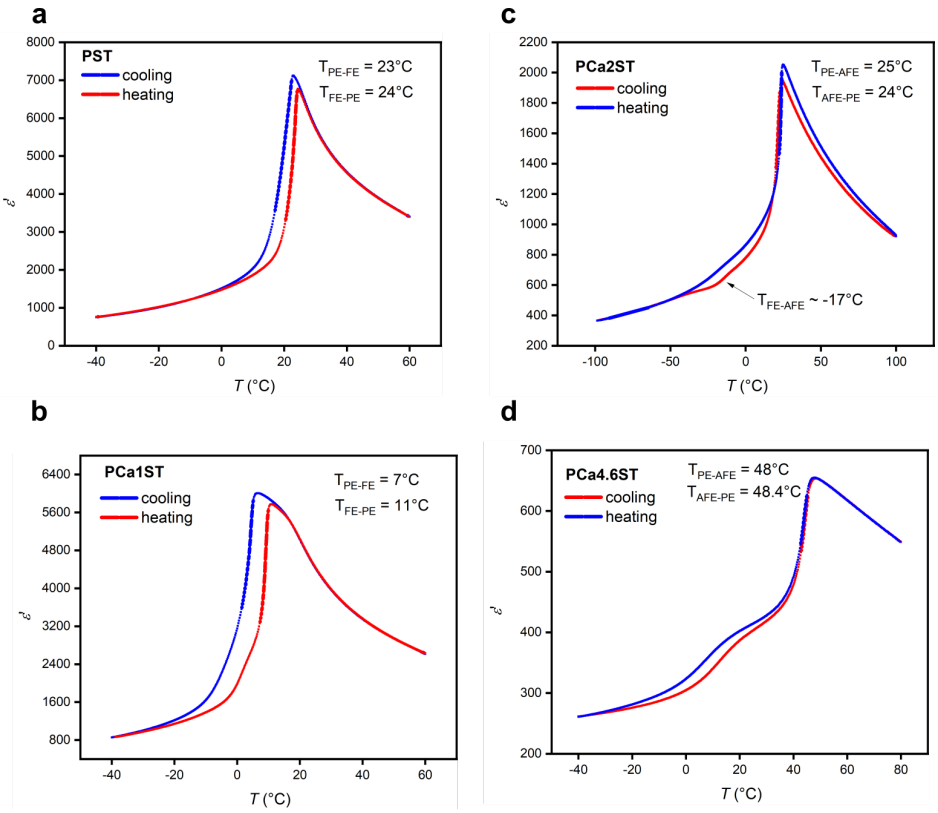

Supplementary Figure 11: **Dielectric measurements of PCaxST.** Dielectric constant ϵ as a function of temperature T. FE, AFE and PE represent, respectively, the ferroelectric, antiferroelectric and paraelectric phases. a) PST b) PCa1ST c) PCa2ST and d) PCa4.6ST.

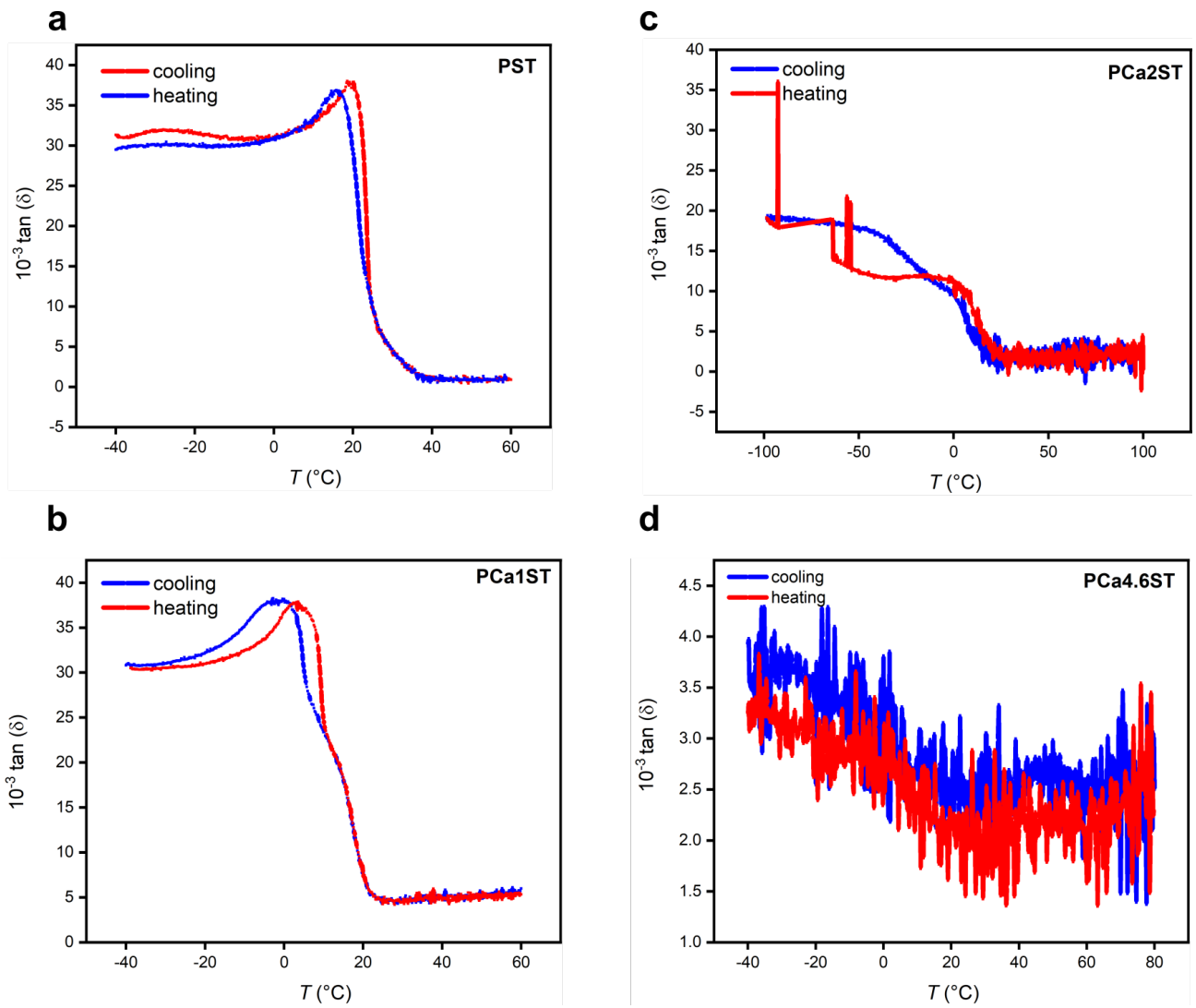

Supplementary Figure 12: **Dielectric losses tan(delta) of PCaxST.** a) PST b) PCa1ST c) PCa2ST, and d) PCa4.6ST.

Supplementary Note 7: DSC measurements on PCa2ST

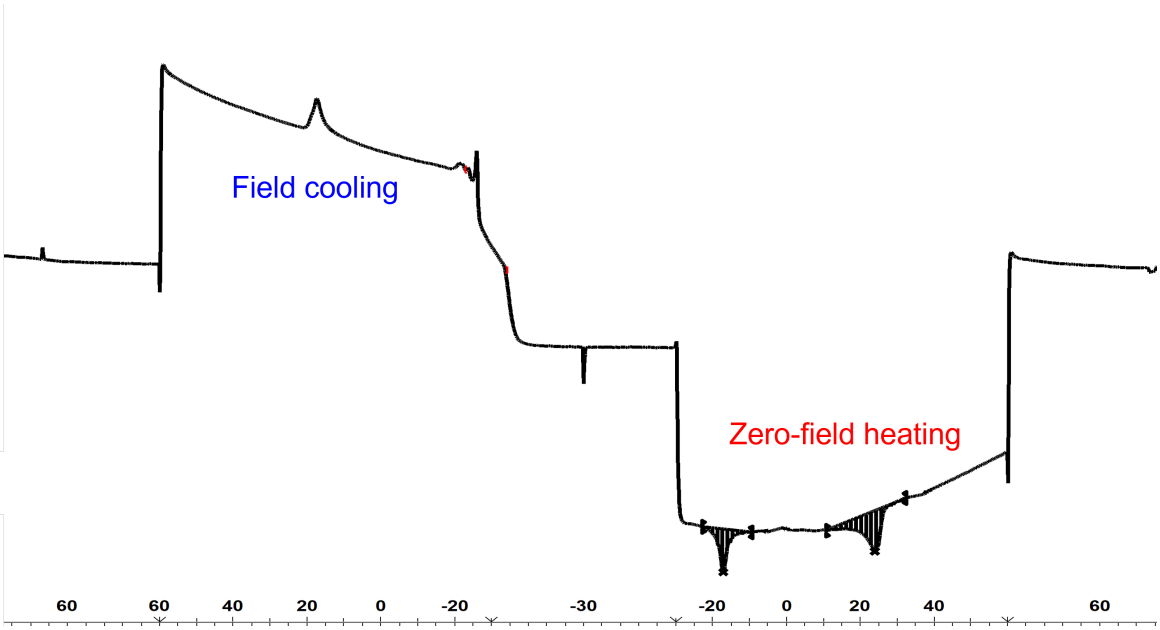

Supplementary Figure 13: **Field cooling and zero-field heating in PCa2ST.**first, field-cooling PCa2ST under a field of 16 kV cm^{-1} and subsequently, zero-field heating PCa2ST.

Supplementary Note 8: Raman spectra of calcium-doped PST

Raman spectra of undoped PST

The phase transition sequence in our five PCaxST samples was studied by Raman spectroscopy (see Methods section). Supplementary Figure 14a shows the temperature dependence of the Raman spectra of PST without electric field, for temperatures ranging from 283 K to 353 K, i.e. across the known FE to PE transition. The most prominent signature of the phase transition is the emergence of a Raman mode around 420 cm^{-1}, as highlighted in the inset. This occurs at 294 K, very close to the transition temperature measured by DSC (297 K). This peak then becomes sharper and more intense with decreasing temperature. Other signatures are present, although weaker, with the emergence of two modes at 125 and 315 cm^{-1}. These observations are overall consistent with previous reports on Raman spectroscopy of ordered PST, as reported in [1, 2]. Perfectly ordered cubic PST has 4 Raman active modes and the transition to the FE phase with symmetry 3m or 3 results in the activation and splitting of 4 polar T_{1u} modes and one silent T_{1g} mode. However, those signatures are quite weak compared to the disorder-induced Raman modes that tend to activate all modes and broaden lineshapes even with a small degree of disorder. In [2], the modes were assigned using atomistic simulations. Based on this study, the Raman mode around 420 cm^{-1} taken here as the main signature of the FE phase can be attributed to a polar O-B-O bending mode and the weaker modes at 125 and 315 cm^{-1} to translation and rotation modes of the octahedra respectively, all having T_{1u} symmetry in the PE phase. Remarkably, all three show a very good agreement with polar LO modes identified from a previous infrared spectroscopy study [3], which tends to confirm this assignment.

We now turn to Raman spectra of PST under an electric field and at different temperatures. Supplementary Figure 14b shows the spectra at increasing electric field at 295 K, just above the transition, in the cubic phase. For low field values, no visible change occurs. Under the application of 4.7 kV cm^{-1}, a peak appears at 420 cm^{-1} that matches the one identified as the signature of the FE phase. This peak gains in intensity until the highest field applied of 7.8 kV cm^{-1}. The other weaker signature of the FE transition are present as well. Upon removal of the electric field, the spectrum reverts back to its initial state. This experiment was repeated at several temperatures up to 308 K and the same behavior was observed, with the critical field shifting to higher values with increasing temperature. Those results are summarized in Supplementary Figure 15 with a *T*-*E* phase diagram showing the boundary between the PE and the FE phase. This phase diagram is in line with the one obtained with DSC (see Figure 3a).

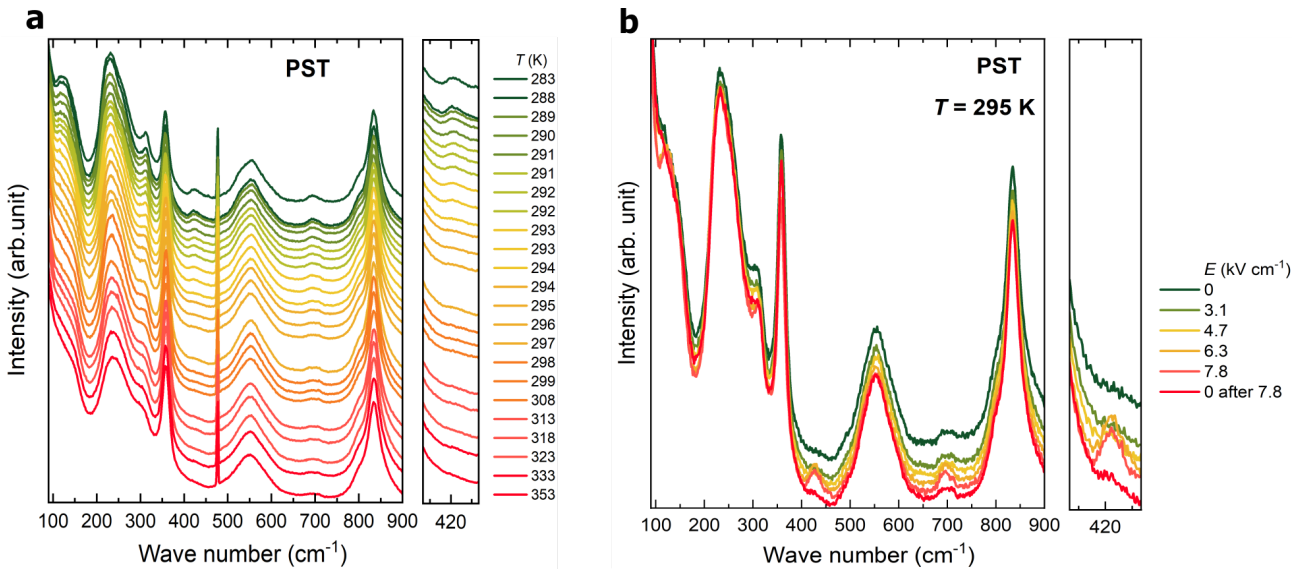

Supplementary Figure 14: **Raman spectroscopy of undoped PST.** (a) Raman spectra of pure PST at temperatures ranging from 283 K to 353 K and zoom in the 420 cm^{-1} Raman shift. (b) Raman spectra of PST pure under different electric fields at 295 K (above the material's transition temperature).

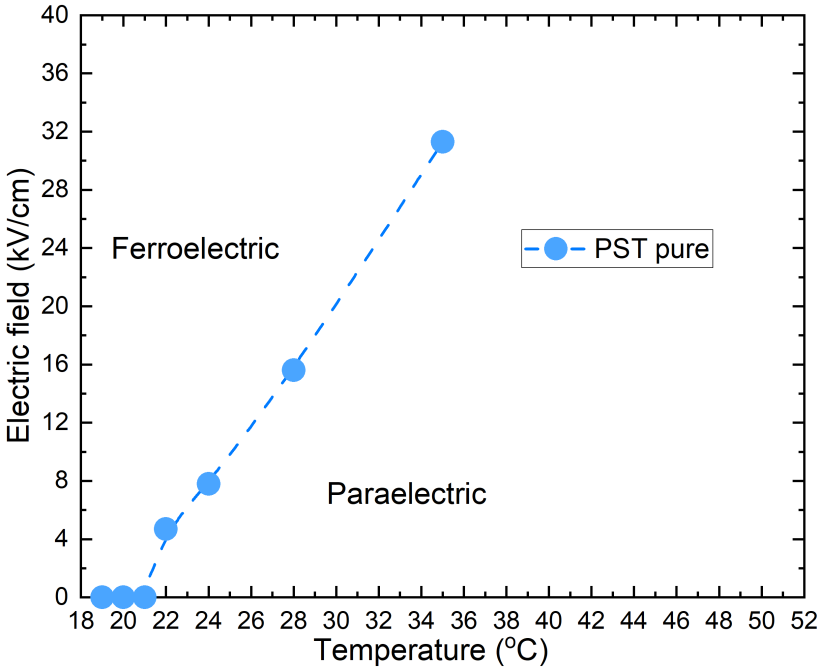

Supplementary Figure 15: **Phase diagram of undoped PST from Raman spectra**

Raman spectra of 2%Ca doped PST

Supplementary Figure 16a shows the Raman spectrum of PCa2ST upon zero-field heating between 283 K and 353 K. Overall, the evolution does not show any strong obvious evidence for phase transitions, and the evolution can at first sight be mostly attributed to thermal broadening. We do observe however the flattening of the peak at the Raman shift 312 cm^{-1} around 295 K, which coincides well with the AFE to PE transition measured in PCa2ST by *P-E* loops and confirmed by DSC. A similar observation is made for the AFE to PE transitions in PCaxST compounds that exhibit such a transition (PCa2ST and PCa4.6ST). Supplementary Figure 18 shows the Raman spectra PCa4.6ST.

The situation is markedly different upon application of an electric field, as shown for PCa2ST in Supplementary Figure 16b. At 223 K, the application of an electric

field of 28 kV cm^{-1} causes the same changes observed in pure PST when inducing the FE phase: strong activation of the polar mode at 420 cm^{-1}, as well as the modes around 140, 310 and 700 cm^{-1}. In fact, the mode at 140 cm^{-1} (BO_3 translations) appears even stronger due to the relatively lower intensity at low frequencies – less quasi-elastic scattering. As shown in the zoom-in of Supplementary Figure 16b and indicated by blue arrows, this signature remains present up to 253 K, where it disappears. Indeed, the appearance of the peak at 420 cm^{-1} indicates the FE phase induced by an electric field in PCa2ST and its disappearance demonstrated the transition of PCa2ST from a FE to an AFE phase which occurs at 253 K. Note that this transition temperature from FE to AFE is close to the transition temperature (258 K) observed by isofield measurements (Figure 3c).

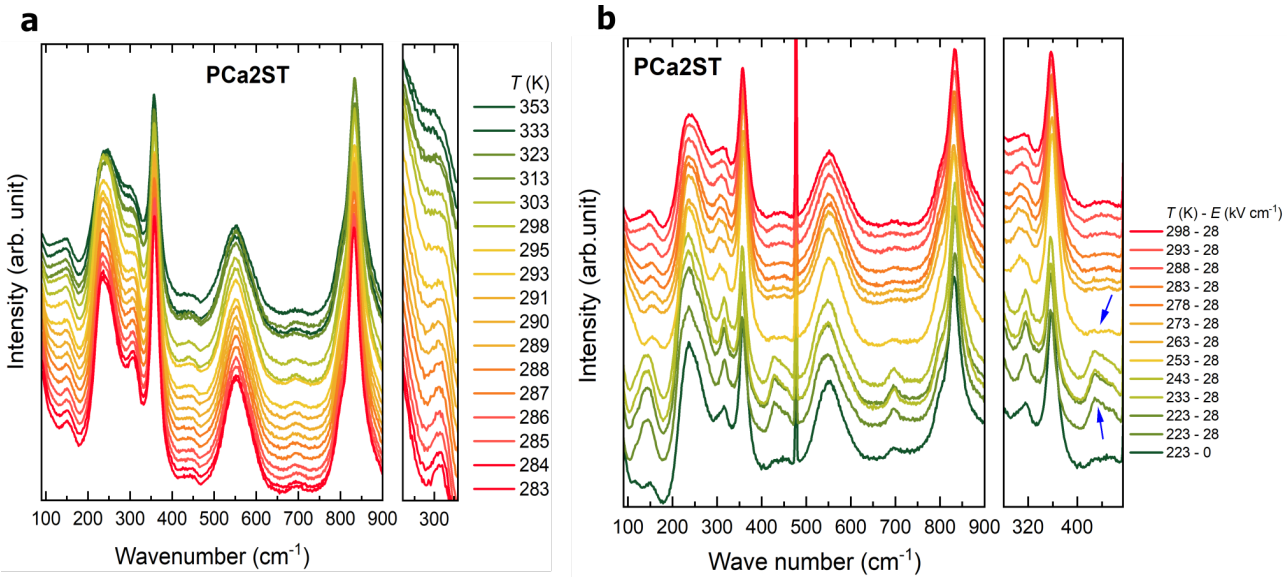

Supplementary Figure 16: **Raman Spectra of PCa2ST.**(a) Raman spectra of PCa2ST at different temperatures and zoom in the 312 cm^{-1} Raman shift. (b) Raman spectra of PCa2ST under the application of an electric field and zoom in the 420 cm^{-1} Raman shift. An electric field of 28 kV cm^{-1} was applied in PCa2ST, subsequently Raman spectra were collected at different temperatures (from 223 K to 298 K). The blue arrows indicate the appearance of a peak at low temperatures (223 K) and at 420 cm^{-1} under the application of the field and the disappearance of this peak at 253 K.

Raman spectra of 4.6%Ca-doped PST

In general, Ca-doping induces some additional disorder that may activate Raman modes. This is demonstrated in Supplementary Figure 17 where all samples are compared at a temperature of 323 K, i.e. in the same PE phase. With increasing Ca concentration, we observe that Raman modes broaden and decrease in intensity; we also observe the emergence of a small bump around 450 cm^{-1}, close to but clearly distinct from the mode at 420 cm^{-1} taken as a signature for the FE phase.

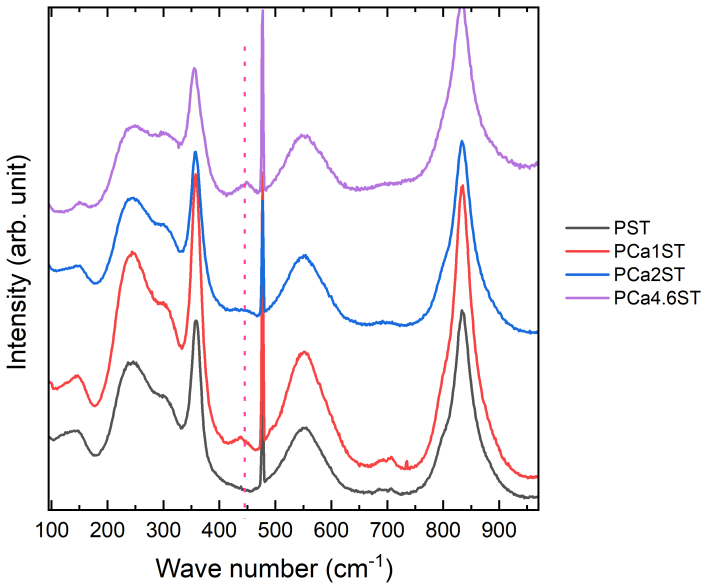

Supplementary Figure 17: **Calcium effect in Raman Spectra at 323 K** Temperature dependence of Raman spectra was carried out in the calcium-doped PST in the same phase (cubic).

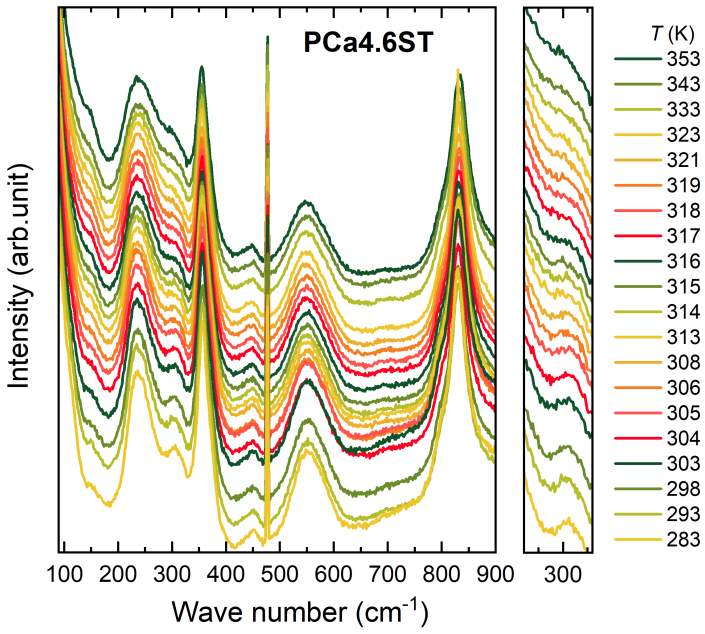

Supplementary Figure 18: **Raman Spectra PCa4.6ST.**

Supplementary Note 9: Piezoresponse force microscopy

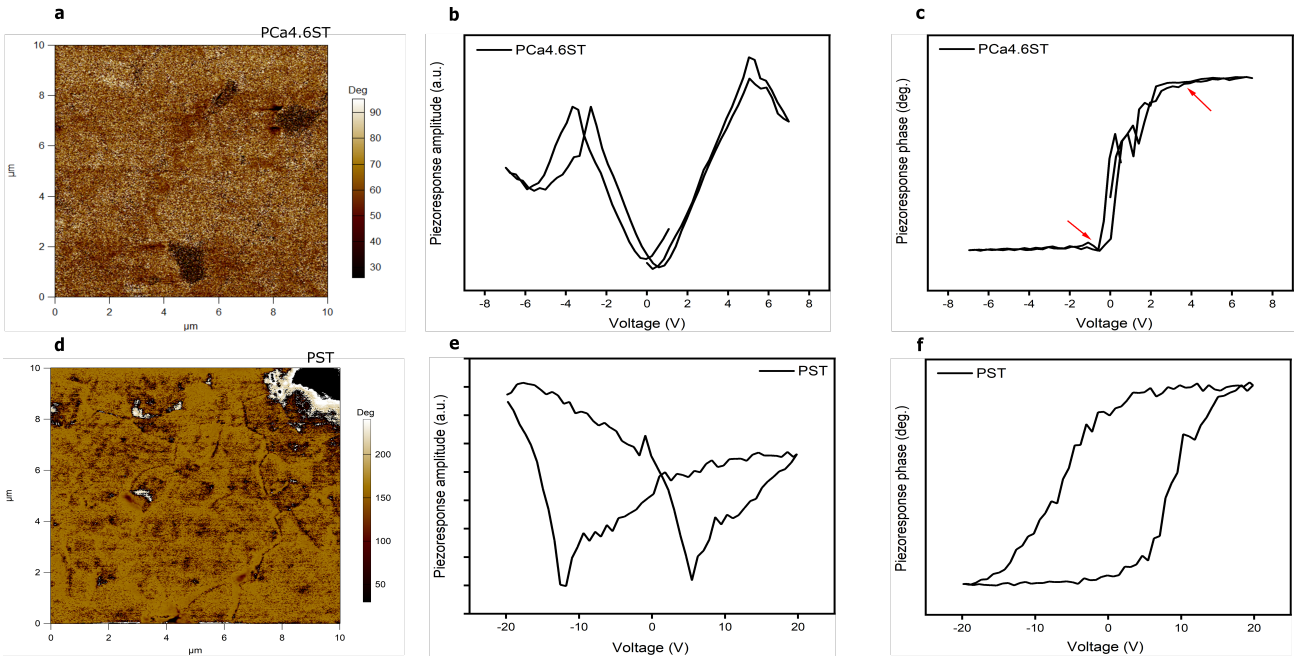

Supplementary Figure 19: **Piezoresponse force microscopy (PFM) of PST and PCa4.6ST.** PFM phase images (a, d), PFM amplitude loops (b, e), and PFM phase loops (c, f). Panels (a–c) correspond to PCa4.6ST, while panels (d–f) correspond to PST.

Supplementary Figure 19 presents the PFM phase images, PFM amplitude loops, and PFM phase loops for both PST and PCa4.6ST samples. For PCa4.6ST, the PFM images under low AC excitation reveal only noise (Supplementary Figure 19a), indicating the absence of piezoelectric activity. In other words, the sample is non-polar. In contrast, the PFM image of undoped PST (Supplementary Figure 19d) shows distinct domain contrast, characteristic of a ferroelectric material. The PFM amplitude loop of PST (Supplementary Figure 19e) exhibits a butterfly-type hysteresis with two minima and a non-zero amplitude at zero bias, indicating a stable remanent ferroelectric polarization. This is confirmed by the PFM phase response

(Supplementary Figure 19f), which shows an hysteresis loop. These features are consistent with ferroelectric behavior and confirm the polarization hysteresis loops previously measured in PST (Supplementary Figure 19a). On the other hand, the bias-on PFM amplitude loop of PCa4.6ST (Supplementary Figure 19b) displays four maxima, which aligns well with the features observed in the polarization–electric field loops. This is further confirmed with a double hysteresis-like loop in the PFM phase response (Supplementary Figure 19c). These are clear signatures of antiferroelectric behaviour as demonstrated in [4] and [5].

Supplementary Note 10: Latent heat of calcium-doped PST

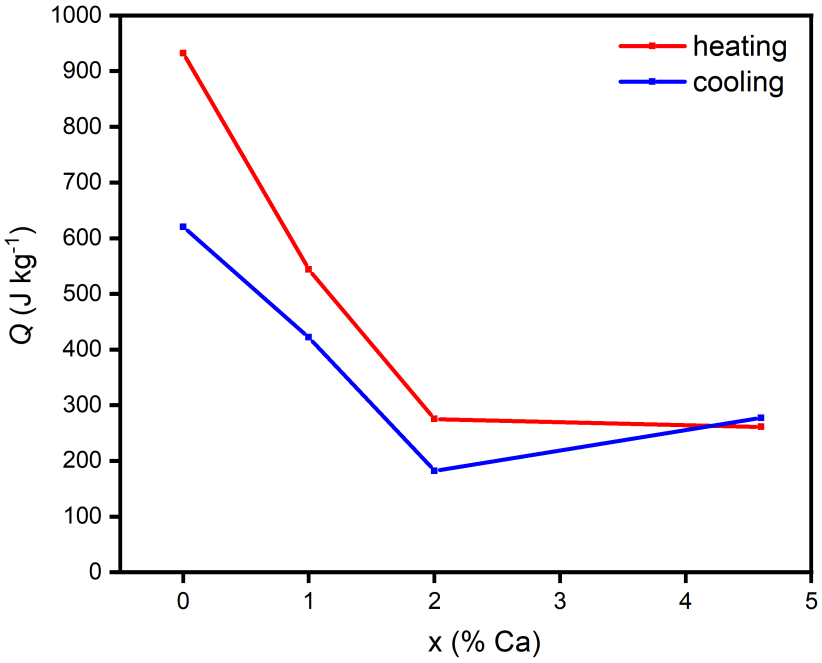

Supplementary Figure 20: **Latent heat Q of calcium-doped PST and a function of calcium content x.**

Supplementary Note 11: Density Functional Theory Calculations

Energies calculations

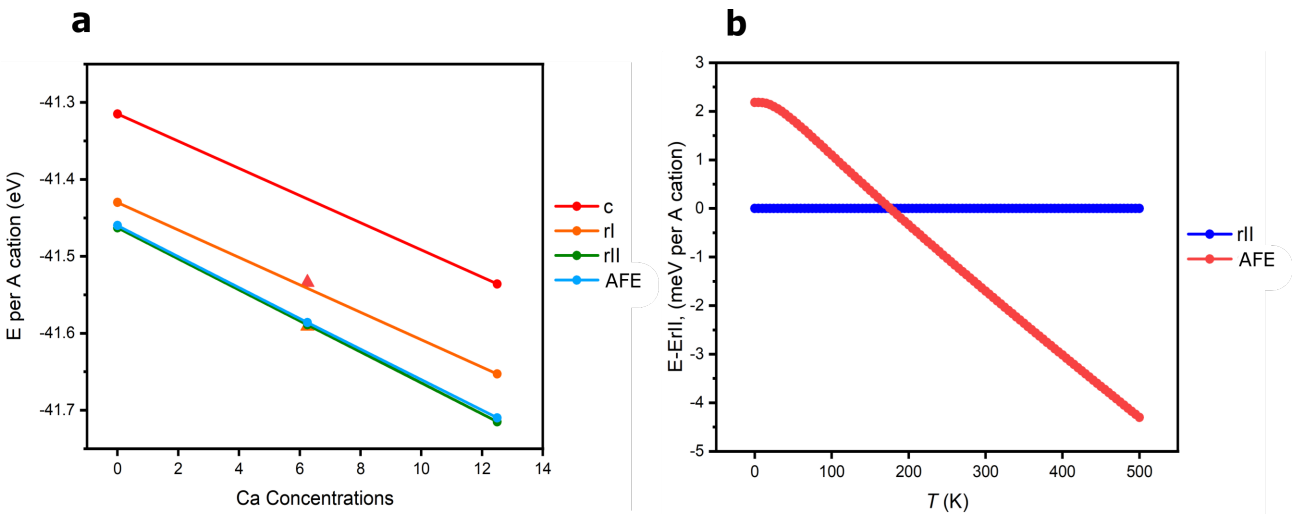

Supplementary Figure 21: **The calculated energies of pure and Ca-doped PST polymorphs.** Panel (a) shows the DFT energies of Ca-doped PST polymorphs as functions of Ca concentration. For 6.25% Ca doping, the c and rI starting configurations relax to lower symmetry phases whose energies are shown with red and orange triangles, respectively (see text for details). The phase indicated by the orange triangle is identical (within numerical error) to rII phase. Panel (b) shows the free energies of rII and AFE phases of pure PST as functions of temperature.

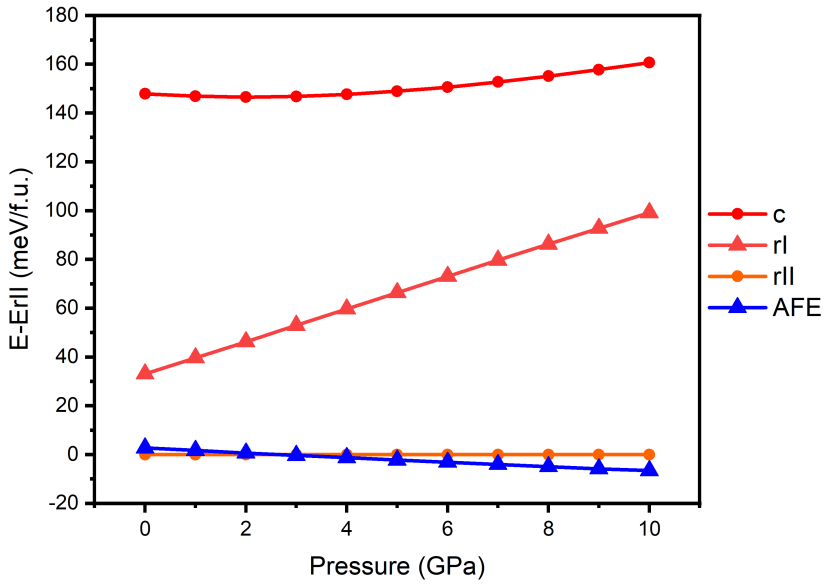

Supplementary Figure 22: **The energies of c, rI, rII and AFE phases as functions of hydrostatic pressure, calculated using DFT.** The energy of rII phase is taken as zero.

Phonons and zero-point contributions

Since the difference in the DFT energies of rII and AFE phases of pure and Ca-doped PST are very small (rII is the lowest energy phase), we check whether the polymorph hierarchy can be affected by zero-point energy (EZP) contributions. Here we focus on the case of pure PST.

First, we compute phonon dispersion for rII and AFE phases. The results are shown in Supplementary Figure 23. One can see that rII phase shows no instabilities, while AFE phase has one unstable phonon branch in the vicinity of the B point with q=(0,0,0.5). Then, we compute EZP for both polymorphs (see Methods for details). The resulting values together with the Kohn-Sham (EKS) energies and the total energies (Etot = EKS + EZP) are summarized in Supplementary Table 2. We find that the addition of EZP to EKS does not change the hierarchy of these polymorphs, and rII remains to be the lowest energy state.

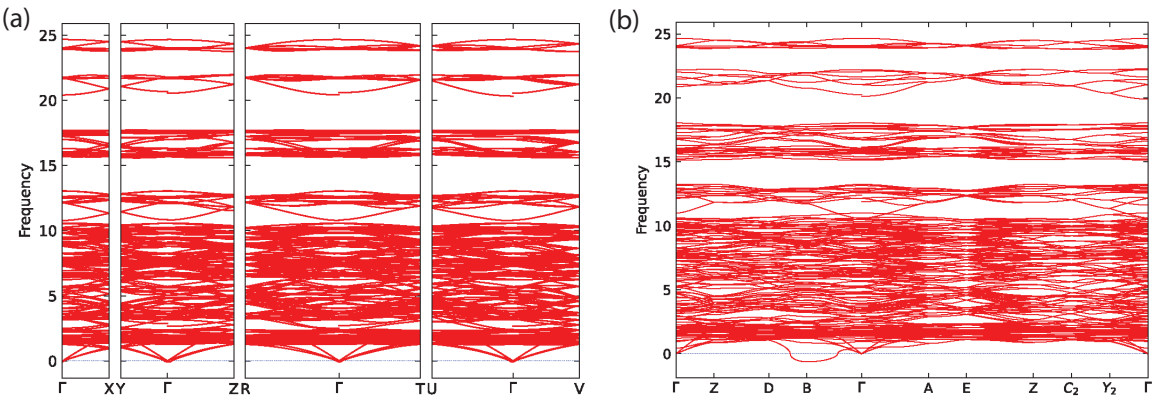

Supplementary Figure 23: **Phonon dispersions of (a) rII and (b) AFE phases of PST.** Phonon frequencies are given in THz.

Supplementary Table 2: **Energy values for different configurations.** The Kohn-Sham energies (EKS), the zero-point energies (EZP) and the total energies (E_{tot}) computed for rII and AFE phases of PST. All energy values are given for 80 atom cell and are in eV.

	$E_{\mathbf{KS}}$	$E_{\mathbf{ZP}}$	$E_{\mathbf{tot}}$
rII	-663.4100	4.2659	-659.1441
afe	-663.3667	4.2576	-659.1091

Effect of Ca doping and hydrostatic pressure on the crystal structure and relative stability of $PbSc_{0.5}Ta_{0.5}O_3$ polymorphs.

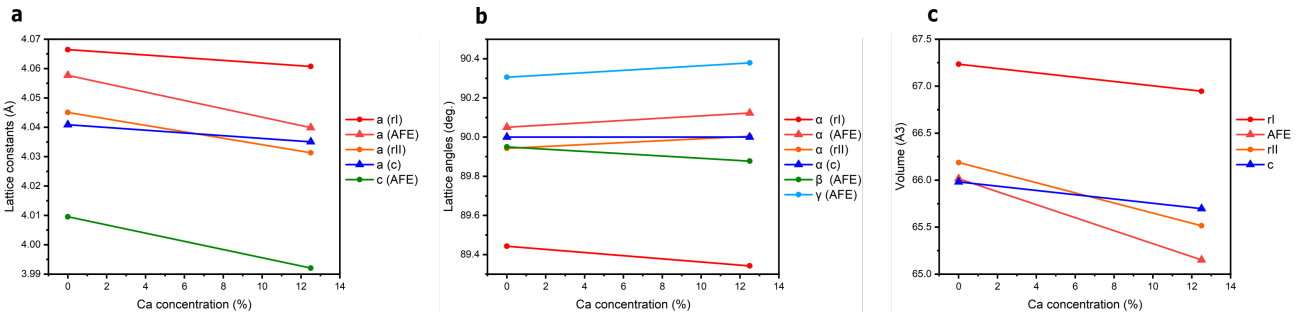

Supplementary Figure 24: **Lattice parameters and volumes of the 5-atom pseudocubic perovskite cell for the c, rI, rII, and AFE phases as functions of Ca doping concentration, as computed using DFT.** Panel (a) shows a, b and c lattice constants; panel (b) - α, β, and γ angles; panel (c) - the volume.

We summarize the lattice parameters of c, rI, rII, and AFE phases of pure and 12.5% Ca-doped PST in Supplementary Table 3 and Supplementary Figure 24. One can see that 12.5% Ca doping leads to an approximately 0.14% reduction in the lattice constants of the c and rI phases (corresponding to a 0.43% reduction in the 5-atom cell volume). For the rII and AFE phases, the lattice parameter reduction is more pronounced: 0.34% and 0.44%, respectively (corresponding to 1.02% and 1.31% reductions in volume, respectively).

The results for the pure PST under hydrostatic pressure are presented in Supplementary Table 4 and Supplementary Figure 25. One can see that an application of P=10GPa reduces the lattice constants of the rI, rII and AFE phases by approximately 1.96% (about 5.7% reduction in volume), while the cubic phase shows a 1.62% reduction in lattice constants (about 4.8% in volume).

By comparing the evolution of the cell volumes under Ca doping and hydrostatic pressure, we estimate that the effect of 12.5% Ca doping corresponds to applying

Supplementary Table 3: Lattice parameters and volumes of the 5-atom pseudocubic perovskite cell for the c, rI, rII, and AFE phases of pure and 12.5% Ca-doped PbSc0.5Ta0.5O3, computed using DFT. a, b, and c are in Å; α, β, and γ are in degrees; V is in Å^3.

	c	rI	rII	AFE
Pure PST				
a	4.0409	4.0665	4.0451	4.0577
b	4.0409	4.0665	4.0451	4.0577
c	4.0409	4.0665	4.0451	4.0095
α	90.000	89.443	89.942	90.050
β	90.000	89.443	89.942	89.950
γ	90.000	89.443	89.942	90.306
V	65.981	67.234	66.188	66.015
12.5% Ca-doped PST				
a	4.0350	4.0607	4.0313	4.0399
b	4.0350	4.0607	4.0313	4.0399
c	4.0350	4.0607	4.0313	3.9921
α	90.000	89.342	90.004	90.123
β	90.000	89.342	90.004	89.877
γ	90.000	89.342	90.004	90.379
V	65.697	66.946	65.515	65.151

0.8 GPa in the c phase, 0.65 GPa in rI, 1.45 GPa in rII, and 1.92 GPa in the AFE phase.

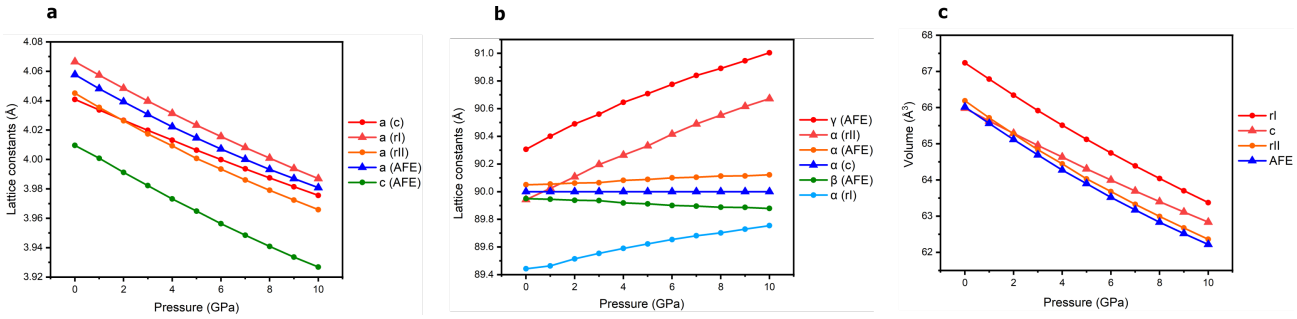

Supplementary Figure 25: **Lattice parameters and volumes of the 5-atom pseudocubic perovskite cell for the c, rI, rII, and AFE phases as functions of hydrostatic pressure, computed using DFT.** Panel (a) shows a, b and c lattice constants; panel (b) - α, β, and γ angles; panel (c) - the volume.

Supplementary Table 4: Lattice parameters and volumes of the 5-atom pseudocubic perovskite cell for the c, rI, rII, and AFE phases of pure PST under 5 GPa and 10 GPa hydrostatic pressure, computed using DFT. a, b, and c are in Å; α, β, and γ are in degrees; V is in Å^3.

	c	rI	rII	AFE
5 GPa				
a	4.0063	4.0233	4.0007	4.0146
b	4.0063	4.0233	4.0007	4.0146
c	4.0063	4.0233	4.0007	3.9649
α	90.000	89.622	90.331	90.088
β	90.000	89.622	90.331	89.912
γ	90.000	89.622	90.331	90.708
V	64.305	65.121	64.028	63.898
10 GPa				
a	3.9755	3.9870	3.9658	3.9808
b	3.9755	3.9870	3.9658	3.9808
c	3.9755	3.9870	3.9658	3.9268
α	90.000	89.755	90.672	90.122
β	90.000	89.755	90.672	89.878
γ	90.000	89.755	90.672	91.004
V	62.833	63.374	62.361	62.217

In Supplementary Figure 21a and 22, we show the relative stability of the considered phases under Ca doping and hydrostatic pressure, as predicted by our DFT calculations. We find that AFE phase becomes more energetically favorable relative to the rII phase at pressures around 3 GPa, whereas rII remains the ground state up to at least 12.5% Ca concentration.

These results indicate that the experimentally observed AFE phase in Ca-doped PST samples (with 2 to 4.6% Ca concentration) cannot be explained solely by the volume reduction caused by doping. It is likely that local relaxation around Ca cations, along with temperature effects, plays a significant role in stabilizing the AFE phase.

Effect of Ca doping and hydrostatic pressure on the distortion mode amplitudes of $PbSc_{0.5}Ta_{0.5}O_3$ polymorphs

To study the effect of Ca doping and hydrostatic pressure on distortion mode amplitudes in the lowest-energy rII and AFE phases of PST, we performed the following analysis. We start with pure PST and consider fully relaxed structures of the c, rII, and AFE polymorphs. For a clearer symmetry-mode decomposition, we replace Sc and Ta cations with a single cation type—Zr. All distortions were referenced to the parent 5-atom cubic perovskite cell of PbZrO3, with lattice constants taken from the fully relaxed cubic PST phase.

Using the ISODISTORT tool [6, 7], we identify the dominant symmetry-adapted distortions that transform the ideal cubic reference into the rII and AFE phases. In the rII phase, these distortions are: 1) Γ_4^- — polar displacement of Zr cations with respect to O anions along the $\langle 111 \rangle$ direction; 2) R_5^- — antiphase tilting ($a^-a^-a^-$) of oxygen octahedra.

In the AFE phase, the dominant modes are: 1) Σ_2 — antipolar displacements of Pb cations along $[11\bar{1}0]$, accompanied by deformation of the oxygen octahedra; 2) R_5^- — antiphase $a^-a^-c^0$ oxygen octahedral rotations.

In Supplementary Table 5, we present the parent-cell-normalized amplitudes A_p of these distortion modes. Here:

$$A_p = A_s \sqrt{\frac{V_p}{V_s}},$$

where V_p and V_s are the primitive parent and supercell volumes, respectively, and A_s is the supercell-normalized amplitude of the mode (root-summed-squared mode-induced displacements within the primitive supercell).

Next, we repeat the same analysis for 12.5% Ca-doped PST and for pure PST under a hydrostatic pressure of 10 GPa. The results are summarized in Supplemen-

tary Tables 5 and 6.

The analysis reveals that the polar distortion (Γ_4^-) in the rII phase is relatively unaffected by Ca doping but is notably suppressed under hydrostatic pressure. The antipolar displacements of the Pb cations (Σ_2 mode) are strongly reduced by both Ca doping and pressure. In turn, the octahedral tilt amplitude increases in the rII and AFE phases under both conditions.

Supplementary Table 5: Computed distortion mode amplitudes (in Å) for the rII phase of pure PST under 0 GPa and 10 GPa hydrostatic pressure, as well as for 12.5% Ca-doped PST. Γ_4^- is the polar distortion mode, and R_5^- is associated with the antiphase $a^-a^-a^-$ oxygen octahedral tilts.

Distortion mode	**PST**	**12.5% Ca-doped PST**	**PST under 10 GPa**
Γ_4^-	0.67126	0.62871	0.34079
R_5^-	0.47156	0.54817	0.55960

Supplementary Table 6: Computed distortion mode amplitudes (in Å) for the rII phase of pure PST under 0 GPa and 10 GPa hydrostatic pressure, as well as for 12.5% Ca-doped PST. Γ_4^- is the polar distortion mode, and R_5^- is associated with the antiphase $a^-a^-a^-$ oxygen octahedral tilts.

Distortion mode	**PST**	**12.5% Ca-doped PST**	**PST under 10 GPa**
Γ_4^-	0.67126	0.62871	0.34079
R_5^-	0.47156	0.54817	0.55960

References

[1]U. Bismayer, V. Devarajan, and P. Groves, “Hard-mode raman spectroscopy and structural phase transition in the relaxor ferroelectric lead scandium tantalate, pb (sc0. 5ta0. 5) o3”, Journal of Physics: Condensed Matter **1**, 6977 (1989).

[2]B. Mihailova, U. Bismayer, B. Güttler, M. Gospodinov, and L. Konstantinov, “Local structure and dynamics in relaxor-ferroelectric $Pb(Sc_{0.5}Nb_{0.5})O_3$ and $Pb(Sc_{0.5}Ta_{0.5})O_3$ single crystals”, Journal of Physics: Condensed Matter **14**, 1091 (2002).

[3]J. Petzelt, E. Buixaderas, and A. Pronin, “Infrared dielectric response of ordered and disordered ferroelectric pb (sc1/2ta1/2) o3 ceramics”, Materials Science and Engineering: B **55**, 86–94 (1998).

[4]H. Lu, S. Glinsek, P. Buragohain, E. Defay, J. Iñiguez, and A. Gruverman, “Probing antiferroelectric-ferroelectric phase transitions in pbzro3 capacitors by piezoresponse force microscopy”, Advanced Functional Materials **30**, 2003622 (2020).

[5]D. Chen, C. T. Nelson, X. Zhu, C. R. Serrao, J. D. Clarkson, Z. Wang, Y. Gao, S.-L. Hsu, L. R. Dedon, Z. Chen, et al., “A strain-driven antiferroelectric-to-ferroelectric phase transition in la-doped bifeo3 thin films on si”, Nano Letters **17**, 5823–5829 (2017).

[6]H. T. Stokes, D. M. Hatch, and B. J. Campbell, *ISODISTORT, ISOTROPY Software Suite*, `http://iso.byu.edu`, Accessed: 2025-08-11.

[7]B. J. Campbell, H. T. Stokes, D. E. Tanner, and D. M. Hatch, “Isodisplace: an internet tool for exploring structural distortions”, Journal of Applied Crystallography **39**, 607–614 (2006).